

Transparent Thiol-ene/Acrylate-Based MicroECoG Devices Used for Concurrent Recording of Fluorescent Calcium Signals and Electrophysiology in Awake Animals

Ágnes Szabó, Miklós Madarász, Zsófia Lantos, Anita Zátanyi, Vindhya Danda, Lisa Spurgin, Connie Manz, Balázs Rózsa,* and Zoltán Fekete*

Shape memory polymers (SMPs) are suitable substrate materials for soft neural interfaces due to their tunable elastic characteristics. The stability and biocompatibility of intracortical SMP probes are demonstrated. In this work, a SMP-based cortical implant capable of recording high-density micro-electrocorticography is utilized in a multimodal neuroimaging scheme. The transparent nature of thiol-ene/acrylate substrate is exploited, and the feasibility of measuring intracranial electroencephalogram and fluorescent GCaMP6 signals with two-photon imaging through the device is presented in mice. The potential influence of the optical properties of the microdevice is investigated using fluorescent microbeads, hippocampal brain slices, and awake animals. It is found that neurites and cell soma can be efficiently detected with sufficient resolution to follow changes in the calcium signal. These chronically implanted devices do not suppress the quality of optical signals exceeding 22 weeks after implantation. These results indicate that thiol-ene/acrylate ECoG is an appropriate tool to combine electrophysiology with two-photon imaging while leveraging the inherent tissue-friendly properties of SMPs.


voltage-sensitive dye imaging catalyzed the development of transparent neural interfaces that enable the application of both modalities. Electrophysiological methods with high temporal resolution are therefore often used in parallel with a non-invasive optical method with high spatial resolution.^[2] Electroencephalogram (ECoG) register neural activity on the cortical surface, circumventing the electrical insulation of the scalp with minimally invasive surgical intervention.^[3] By using of ECoG instead of the non-invasive electroencephalography (EEG) the difficulty to achieve efficient electrode-skin impedance^[4] can be overcome. Two-photon microscopy is a laser-scanning, multifocal technique that typically collects fluorescent light from a single location.^[5] Since two photons combine their energy during measurement, they are less harmful to biological tissues than the

1. Introduction

Multimodal measurements have emerged as the functional and structural observation of the brain is required to understand the complex mechanism of neuronal ensembles. Electrophysiology is still used as a gold standard to interrogate brain activity by measuring the chemical and electrical signals of the living neurons.^[1] However, the advent of new optical characterization tools like optogenetics, calcium imaging, or

single-photon techniques. The two-photon calcium imaging is an efficient way to monitor the calcium-binding kinetics with a highly precise morphological image.^[6] This method uses the fact, that in the living cells most of the depolarizing signals are in connection with the Ca²⁺ influx, because of the voltage-gated Ca²⁺ channels.^[7] Optogenetics provides molecular tools to selectively manipulate neuronal activity with light.^[8] This technique uses genetic engineering to insert photosensitive protein channels into a specific population of neurons.^[9]

Á. Szabó, Z. Lantos, A. Zátanyi, Z. Fekete
Research Group for Implantable Microsystems
Faculty of Information Technology and Bionics
Pázmány Péter Catholic University
Budapest 1083, Hungary
E-mail: feketek.zoltan@itk.ppke.hu

 The ORCID identification number(s) for the author(s) of this article can be found under <https://doi.org/10.1002/admi.202200729>.

© 2022 The Authors. Advanced Materials Interfaces published by Wiley-VCH GmbH. This is an open access article under the terms of the Creative Commons Attribution License, which permits use, distribution and reproduction in any medium, provided the original work is properly cited.

DOI: 10.1002/admi.202200729

Á. Szabó, Z. Lantos
Roska Tamás Doctoral School of Sciences and Technology
Faculty of Information Technology & Bionics
Pázmány Péter Catholic University
Budapest 1083, Hungary
M. Madarász
János Szentágothai PhD Program of Semeleweis University
Budapest 1088, Hungary
M. Madarász, B. Rózsa
Laboratory of 3D functional network and dendritic imaging
Institute of Experimental Medicine
Budapest 1083, Hungary
E-mail: rozszabal@koki.hu
V. Danda, L. Spurgin, C. Manz
Qualia Labs, Inc.
Dallas, TX 75252, USA

These channels can be controlled with the delivery of light in millisecond-scale.^[18]

Recent advances in materials science have had a transformative effect on the fabrication of microimplants that enable the simultaneous application of electrical recording and optical imaging.^[10] A growing number of potential substrate materials have been proposed to create transparent ECoG devices. Among transparent substrates, polyimide,^[11] SU-8,^[12] Parylene C,^[13] Parylene HT,^[14] polydimethylsiloxane (PDMS),^[15] and many others have been proposed to hold functional layers of transparent neural implants, with many of these materials already tested experimentally. Polyimide and sputter-deposited indium-tin-oxide (ITO) has been used to create a μ ECoG to record the anatomical map of the visual cortex with intrinsic optical imaging while following the electrophysiological response to visual stimulus.^[11] A polyimide and gold nanonetwork (Au NN)-based transparent ECoG was proposed to simultaneously record in vivo activity and perform optogenetic stimulation with channelrhodopsin-2.^[16] Transparent Au nanogrid electrodes and microscale inorganic light-emitting diodes (μ -ILEDs) have been encapsulated in a flexible SU-8 substrate for simultaneous electrophysiological recording and optical modulation.^[12] Recently, optogenetically evoked ECoG activity in the rat visual cortex was demonstrated in vivo, using a conductive, antireflective, transparent, and flexible μ ECoG array of PEDOT:PSS–ITO–Ag–ITO multilayer thin films on Parylene C.^[13] Since we aim to use our device in combination with fluorescent microscopy, low autofluorescence is an also important requirement that should be fulfilled by the choice of substrate material. Polyimide, PDMS, PMMA, polycarbonate, and Parylene have been tested.^[17] High autofluorescence or background fluorescence hinders the recording of high resolution images on fluorescently labeled cells. While the popular ECoG material, polyimide shows the worst autofluorescence properties, other candidates like Parylene are most suitable to be applied as transparent substrates. For instance, Parylene HT, a transparent substrate with low-autofluorescence, combined with ITO, has been used to perform two-photon imaging and cortical electrophysiology in freely moving animals.^[14]

In addition to metallic alloys, graphene-based arrays are also extensively developed and applied experimentally, to combine with optogenetic modulation and two-photon imaging,^[18] or wide-field calcium epifluorescence imaging.^[19]

The popularity of graphene can be explained by a higher signal-to-noise ratio (SNR) and reduced electrical interference noise compared to gold electrodes.^[20] Although its electrochemical impedance is high, it can be decreased by electrodeposition of platinum nanoparticles onto the surface doped in 35% nitric acid.^[21]

The impedance of electrodes inherently depends on their size, with smaller electrodes having higher impedance. To overcome this problem, Quiang and colleagues created bilayer-nanomesh microelectrode arrays (MEAs)^[22] with Au/PEDOT:PSS material combination, resulting in single-neuron-sized microelectrodes with low impedance. In vivo validation proved that the bilayer-nanomesh MEAs are fully compatible with two-photon Ca^{2+} imaging.

Besides the ability of these devices to meet the demands of both intracranial electrophysiology and artifact-free optical

imaging or optical stimulation of genetically incorporated proteins through the transparent device, biocompatibility in long-term, chronic experiments are rarely investigated. Minimizing the neural response improves the longevity of implants in multimodal neuroimaging schemes. The application of responsive polymers may be a key technology in this endeavor.^[17,18] These materials reduce the mechanical mismatch at the tissue and neural interface, therefore reducing the inflammatory response.^[24] Thiol-ene-based flexible devices have been characterized previously both electrically^[25] and optically.^[26] Thiol-ene has high optical transparency (above 85% @ 550 nm) with a refractive index of about 1.54,^[27] and it has been used as the substrate in wearable LED devices.^[28] These promising results make transparent shape memory polymers (SMPs) good candidates to fabricate neural interfaces designed for cortical electrophysiology and simultaneous two-photon imaging.

In our previous paper,^[23] we presented the change of the Young's modulus of a thiol-ene/acrylate neural probe, which decreased from 2 GPa to 300 MPa upon immersion into room temperature saline solution and heating the medium up to 37 °C. Later, we proposed the first thiol-ene/acrylate-based μ ECoG device and confirmed its electrical stability and biocompatibility in chronic experiments in mice.^[29] Based on our histology study targeting astrocyte (GFAP staining) evolution and neuronal survival after 80 days of implantation on average, there was no significant difference in the average number of cell nuclei below the implant, while the difference of fluorescence intensity of astrocyte markers showed a mild scar evolution. After these positive findings, here we present the optical characterization and in vivo validation of a thiol-ene/acrylate-based μ ECoG array with gold and sputtered iridium oxide film (SIROF) conductive layers in a two-photon calcium imaging scheme. Optical qualities of the μ ECoG were tested using fluorescent microbeads and automatically detected neurites in vitro acute brain slices. Long-term performance of the μ ECoG device was assessed with chronic two-photon calcium imaging. Single neurons remained active and distinctive even 22 weeks after implantation.

2. Experimental Section

2.1. Microfabrication

The soft and flexible μ ECoG device used in this study was designed to cover a 2.4 mm by 3 mm area with 31 symmetrically arranged gold recording sites. The first and seventh rows of the array had three recording sites each, while the five rows in between them had five sites each, all equally distant from neighboring sites. Site diameter was 115 μ m and inter-site distance was 400 μ m. The thickness of the composite device was 18 μ m. The microfabrication process was performed at Qualia Labs, Inc. based on the micromachining scheme of the intracortical probe published earlier.^[23] The layer composition is the following: a thiol-ene/acrylate substrate of 7 μ m already spin coated on top of a silicon handle wafer was coated with 2 μ m Parylene C. Since the composition of thiol-ene/acrylate that was used exhibit a water uptake less than 3%, this might lead short-circuits along the gold wiring. To avoid this failure,

a thin Parylene C layer was applied to protect the conductive layer from this effect. This way, the beneficial mechanical property of the tissue-device interface to foreign body response was exploited, while functionality was maintained even during chronic use. It should be noted that the presence of metal tracks and their Parylene C capping did not influence the characteristic softening behavior of the substrate, and lead to a minimal change in bending stiffness as located along the neutral axis of the whole multi-layer structure. Conductive traces were then photolithographically patterned on a 400 nm thick gold layer. The top encapsulation layer consisted of another 2 μm thick Parylene C and a 7 μm thick thiol-ene/acrylate layer, which was removed above the recording sites and bonding pads using reactive ion etching in oxygen plasma (Device A). On some devices, an additional 300 nm thick sputtered iridium oxide (SIROF) layer was patterned on top of the exposed recording sites (Device B). The devices were completely released from the silicon handle wafer with tweezers after immersion in DI water; they were mounted on a through-hole Omnetics connector (A79022-001, Omnetics Connector Corp., USA). Interconnection between the integrated conductive traces and the connector pins was carried out using a two-component conductive epoxy (CW2400, Chemtronics, USA), dried at room temperature for 24 h. To isolate the through-hole joints, a final layer of Araldite 1401 adhesive (Huntsman Advanced Materials, TX, USA) was applied and cross-linked without using any thermal annealing processes. The final device is shown in **Figure 1A**.

2.2. Electrical Characterization

In order to validate long-term electrical performance of the proposed material composition in μECoG devices, Bode plots were recorded from each functional electrode using electrochemical impedance spectroscopy (EIS) technique and Gamry Reference 600+ Potentiostat (Gamry Instruments, Warminster, PA, US). In a three-compartment electrochemical cell miniature, an Ag/AgCl electrode was used as a reference electrode (ET072-1, eDAQ Pty Ltd., Australia) and a platinum wire as a counter electrode. 31 gold (Device A) recording sites were connected as working electrodes one by one. The electrolyte was 0.01 M phosphate buffered saline (PBS) solution (P4417, tablet diluted in 200 mL distilled water, pH 7.4, Merck KGaA, Germany). The frequency range was between 1 Hz and 10 kHz. Bode plots were recorded immediately after arrays were submerged in the electrolyte and thereafter on a daily basis for 16 days. All experiments took place inside a grounded Faraday cage to suppress environmental noise.

2.3. In Vitro Characterization of Optical Performance

To detect the effects of the μECoG on two-photon imaging, fluorescent microbeads were used. Beads were encased between glass slides and No. 1 size cover glasses. Arrays were placed right on top of the cover glasses and held down with harp slice grids (HSG-5AD, ALA Scientific Instruments), to prevent the surface tension of water immersion to lift the arrays. The same beads, with 6 μm nominal size,

were in the focus of the microscope in both cases. The size of the captured beads was calculated with a custom MATLAB (Mathworks) algorithm, detailed in Section 2.6, and compared (**Figure 2C**).

For in vitro optical characterization, three thy1-GCaMP6f (FVB/Ant) transgenic mice (aged 22, 23, and 103 days) were used. Preparation of acute brain slices was carried out as described previously.^[14] Briefly, 350 μm thick horizontal hippocampal slices were collected and examined under continuous artificial cerebrospinal fluid (aCSF) perfusion^[30] and oxygenation. Images of hippocampal regions were taken with or without the device covering the slice and processed with a custom algorithm described in Section 2.6.

Two-photon microscopic measurements of fluorescent microbeads and in vitro transgenic brain slices were carried out with galvanic scanning on a Femto2D – DualScanhead microscope (Femtonics Ltd.) using a Chameleon Ultra II laser at 910 nm as laser source and equipped with a 16 \times objective (CFI75 LWD, Nikon), PMT (H10770B-40, Hamamatsu), and dichroic mirror (700dcxr, Chroma Technology).

2.4. Surgery

All procedures were carried out according to national guidelines (PE/EA/776-5/2021). Three adult C57BL/6J male mice were used. Mice were subjected to cortical microinjections of AAV1.Dlx-GCaMP6f and μECoG device implantation, which, along with detailed surgical protocol, were described in detail previously.^[14,29] Briefly, mice were anesthetized, the skin on the head removed and the skull cleaned. A rectangular craniotomy, $\approx 2.6\text{-by-}3.2$ mm in size, enclosing the viral injections ([AP,ML] 1: [-1.6, -2.0], 2: [-2.4,-2.0]) was performed with a 0.3 mm drill bit. The dura was removed, the μECoG device was placed directly on the brain surface and covered with custom-cut rectangular cover glasses to hold the device on the brain surface and to seal the craniotomy. Two cover glasses, one smaller ($\approx 2.6\text{-by-}3.2$ mm) to fit into the craniotomy, and one larger ($\approx 3.2\text{-by-}4.0$ mm) to lay onto the edge of the craniotomy were used. The cover glasses were glued together before surgery with optical adhesive (Norland 71) for easier handling. The cover glasses, the device connector, and a reference electrode over the cerebellum were adhered with quick curing glue and dental cement. A headbar was fixed anterior to the craniotomy with Superbond (Tentang CTBA). Mice were allowed to rest for at least 5 days before measurements.

2.5. In Vivo Recordings (Two-Photon Imaging and Electrophysiology)

In vivo measurements started at least 5 days after implantation and continued for 22 weeks at most. During measurements, awake mice were head-fixed on a circular treadmill but were otherwise freely moving. The movement of the treadmill (running) was also recorded. Cells expressing GCaMP6f located under the μECoG device were imaged with resonant scanning at 31 Hz using the two-photon calcium imaging system described in Section 2.3. Electrode impedance and electrophysiological data were recorded from 31 recording

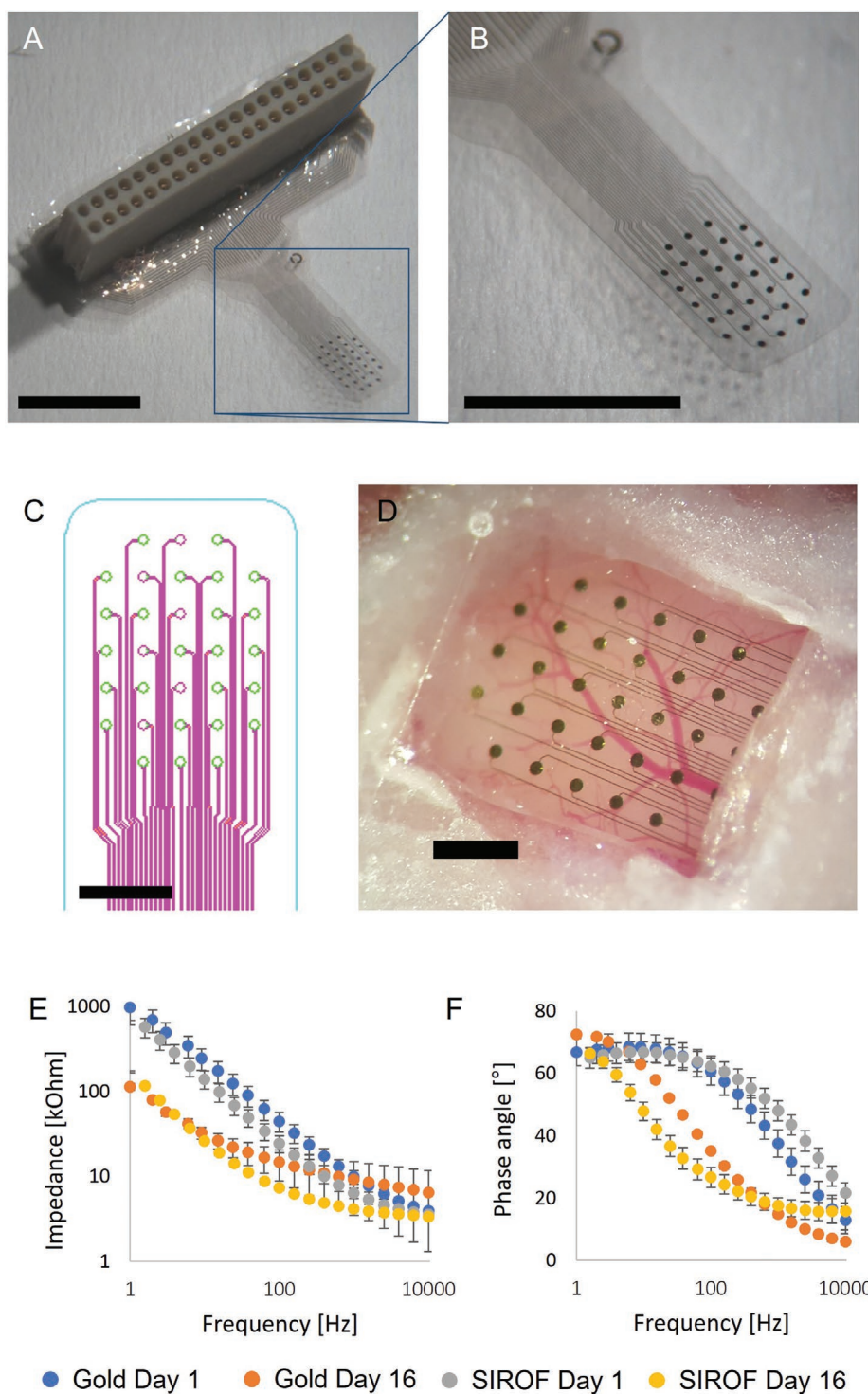


Figure 1. A) Photograph of the finished device. Scale bar is 5 mm. B) Magnified view of the contact points. Scale bar is 5 mm. C) Layout of the device. Scale bar is 1 mm. D) Close up image of the in vivo craniotomy. Scale bar is 1 mm. E) Mean magnitude of impedance and F) phase angle of μ ECoGs with gold or SIROF electrodes after encapsulation (Day 1), and after a 16-day long soaking test including standard deviation.

sites sampled at 2 kHz using a 32-channel RHD recording headstage and RHD2000 Evaluation system (INTAN Technologies) and filtered between 2 and 150 Hz. Impedance was measured in vivo with the built-in feature of the open source

INTAN Technologies RHD Evaluation system. Impedance was measured before data recordings, at a frequency of 1 kHz. It should be noted that during in vivo measurements individual device properties as well as difference in the equivalent

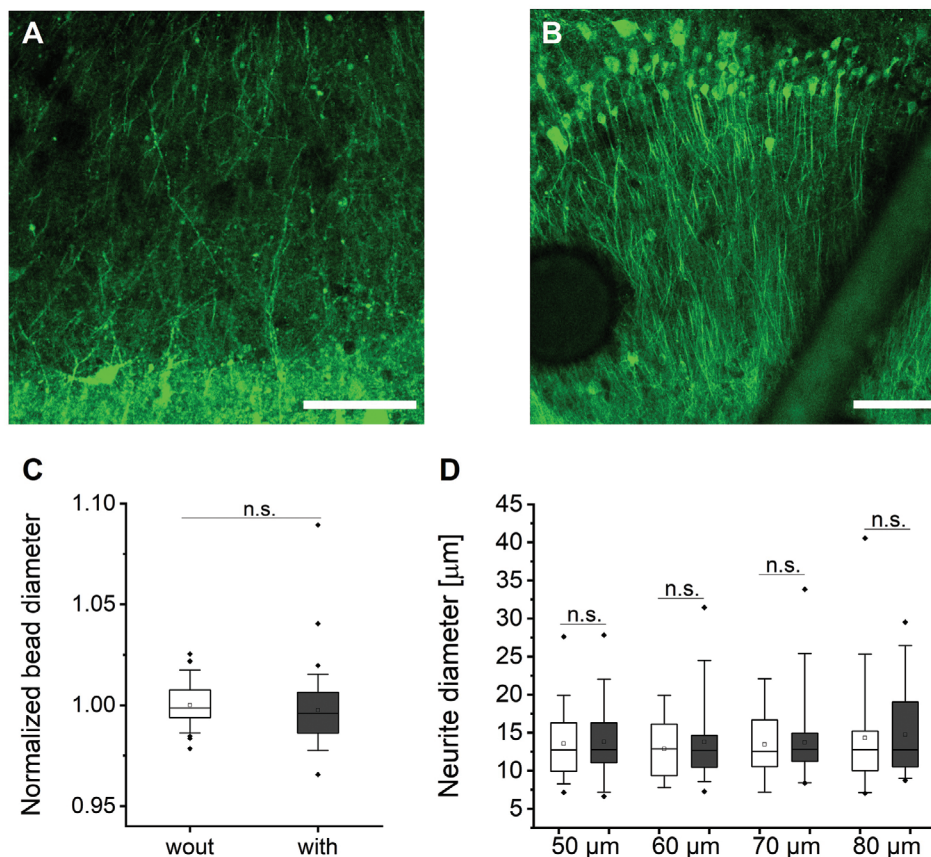


Figure 2. Representative images of hippocampal regions A) without and B) under the μ ECoG device. Scale bars are 100 μ m. C) Diameter of the same beads without ($n = 68$) and with ($n = 68$) the μ ECoG device covering them. Values are normalized to the mean diameter of the beads without the device ($5.67 \pm 0.0066 \mu$ m). D) Diameter of neurites measured on in vitro slices from the same field-of-view (FOV) but at different depths. Empty box plots, measurements without device cover; filled box plots, device on the slice. Boxplot whiskers are 5th and 95th percentiles, \blacklozenge are the outliers.

circuit parameters of the measurement system may lead to the increase of the measured site impedances. To properly filter out failed electrode sites, an upper limit of 250 k Ω of site impedance was determined. Above this value, measured signals were discarded.

2.6. Data Analysis

Fluorescent microbeads were captured with MES (Femtonics Ltd.) recording software and analyzed with MATLAB. Beads were detected with a custom algorithm based on the Circular Hough Transform.^[31] The uncertainty of the bead edge was overcome with thresholding (im2bw function with level value 0.005). The same microbeads were captured without and under the μ ECoG, so the effects of the device on optical performance can be determined by statistical tests on bead sizes. The diameters of the beads were compared with Student's paired t -test with 0.05 α value with software OriginPro (OriginLab).

In vitro images were captured with MES and analyzed with MATLAB. First, the images were cut to four overlapping tiles and the fluorescence values were normalized to be between 0 and 1, in order to achieve more accurate detection. These tiles were segmented differently based on their average intensity.

If the mean intensity of the tile was larger than 0.1, adaptive thresholding was used with a sensitivity value of 0.1. Otherwise, a global threshold was used, based on Otsu's method.^[32] The tiles were structured with morphological operations (bwareafilt, strel, imopen, imclose) for neurite detection. After this, a watershed algorithm was used to separate the detected objects. Neurites were detected automatically by determining the circularity of detected objects, which was determined by using the circularity field of the regionprops function. A detected object was determined as neurite if this metric was lower than the threshold level (0.1). After the detection, the detected objects from the tiles were mapped to their original coordinate on the image, and duplicates were filtered out. The statistical comparison was performed on the neurite diameter (minor axis length) with Student's two-sample t -test with 0.05 α value with software OriginPro.

In vivo resonant scanning measurements of 3–10 min length were recorded with MESc (Femtonics Ltd.) and analyzed in MES and MATLAB. Time-series image stacks were averaged across time, and cell bodies on the averaged images were automatically detected with the same detection algorithm, but different metric threshold, used on in vitro images. A detected object was determined as a cell body if the circularity was larger than the threshold (0.4). Detected cells were used as regions-of-interest

(ROI) to extract cellular calcium activity. To illustrate cell activity, raw fluorescence of ROIs was Gauss filtered ($\sigma = 5$) and converted to relative fluorescence change as $\Delta F = \frac{f_i - f_0}{f_0}$, where f_0 is the mean of the lowest 12.5% data points of an individual trace, and f_i are the individual intensity values over time.

For comparison of measurements, the original pixels of the detected cell bodies were averaged for each cell (f) and the intensity change values were calculated as $\frac{f - f_0}{f_0}$ where f_0 is the mean of the lowest 12.5% data points of the averaged time-series stacks.

The results were represented with boxplot figures, where the whiskers are the 5th and 95th percentiles, the outliers are represented with symbol \blacklozenge , and the mean value with \square . The figures were created by OriginPro.

Electrophysiological data analysis was performed with a custom-made MATLAB program. The treadmill movement was used to identify resting periods in the measurements. A 30 s long segment when the subject remained immobile was selected from every measurement. The SNR was calculated based on the work of Lecomte et al.^[33] as $SNR = \frac{A}{2 * SD_{noise}}$,

where A is the peak-to-peak value of the filtered data. The noise was derived from the difference between the raw data and the filtered data, and its standard deviation was calculated to determine the SNR. The filtered data was created by using a 1 Hz high pass filter (fourth order Chebyshev filter with 30 dB attenuation) and a 140 Hz low pass filter (fourth order Chebyshev filter with 30 dB attenuation). During in vivo recordings, an upper impedance limit was adopted as an acceptance criterion, 500 k Ω . Above this value, the electrode was considered nonfunctional.

3. Results and Discussion

3.1. Electrochemical Performance

Results of EIS measurements at the frequency range of 1 Hz to 10 kHz are summarized in Figure 1E,F. The initial average impedance in the case of gold electrodes (Device A) was 9.9 ± 1.8 k Ω at 1 kHz and decreased to 9.2 ± 5.7 k Ω after 16 days. In the case of SIROF recording sites (Device B), impedance was 6.4 ± 0.9 k Ω at 1 kHz, which decreased to 4.1 ± 0.3 k Ω on the first day. These values remained stable during the rest of the experimental period (16 days). In the case of Device A, only the number of functional electrodes decreased by four (from 30 functional sites to 26), which is associated to the unstable connection of related bonding pads to the pins of the Omnetics connector. Changes in impedance were likely due to the water uptake of the SMP material, similarly to the cases of our previously monitored devices composed of thiol-ene/acrylate.^[23,29] The equivalent circuit parameters derived from Randles' model (Figure S1, Supporting Information) of thiolene-acrylate ECoGs during the 16 days long experiment are presented in Figure S2, Supporting Information. This data supports the reliability of the proposed material composition, and microfabrication processes.

3.2. Fluorescent Microbeads

To detect the effects of the μ ECoG on two-photon imaging, 68 of the same fluorescent microbeads on glass slides were captured with and without the device covering the microbeads. Figure 2C shows boxplots of bead diameters. Represented values are normalized to the mean diameter in absence of the device (5.6651 ± 0.0066 μ m). The calculated Student's paired sample t -test at 0.05 significance level showed no significant difference between the bead diameters in the presence and absence of the device ($t(67) = 1.08$, $p = 0.29$, difference between means: 0.0142 μ m). This confirms our hypothesis that our SMP-based μ ECoG device does not cause considerable optical distortion.

3.3. Acute Brain Slices

Quality of two-photon calcium imaging and the presence of optical distortions were further tested with acute brain slices in vitro. To investigate the possibility of imaging fine neural structures, neurite diameter was measured with and without the μ ECoG device. Neurites were detected on images of hippocampal regions, where the plane of the image was parallel to the neurites, to maximize the number of samples. Figure 2A,B shows hippocampal regions without and with the μ ECoG. Figure 2D shows the diameter of detected neurites from the same field-of-view (FOV), but at different depths from the slice surface. The detection algorithm was able to detect 81 neurites on images without the device and 112 neurites with the device present. There was no significant difference between the neurite diameters without and with the μ ECoG in the same FOV at $\alpha = 0.05$. (Student's two-sample t -test, $z = 50$ μ m: $n_{w/out} = 21$, $n_{w/ith} = 28$; $t(47) = -0.18$, $p = 0.85$; $z = 60$ μ m: $n_{w/out} = 17$, $n_{w/ith} = 28$; $t(143) = -0.61$, $p = 0.55$; $z = 70$ μ m: $n_{w/out} = 16$, $n_{w/ith} = 33$; $t(47) = -0.18$, $p = 0.86$; $z = 80$ μ m: $n_{w/out} = 27$, $n_{w/ith} = 23$; $t(48) = -0.25$, $p = 0.81$).

With these in vitro measurements, we show that in the well-investigated hippocampus, even fine dendrites can be visualized in the presence of our device without distortion in the two-photon images.

3.4. In Vivo Performance

Stability of the recording sites was monitored before and after the implantation process up to the point where the animals were sacrificed. This measurement relied on impedance testing, which is able to indirectly inform us on device failure, including any mechanical damage (cracking, delamination, leakage). SNR was also calculated.

In the case of Device A, there was a decrease in the impedance after the surgery (Figure 3A), but there was no significant change between week 2 and week 11 (Student's paired sample t -test at $\alpha = 0.05$: $t(9) = 0.12$, $p = 0.91$). At the same time, the SNR slightly increased (Figure 3B). "Precranio" values are derived from measurements in saline, while the rest of the data are collected after implantation. Health condition of mice implanted with Device A required earlier termination of the

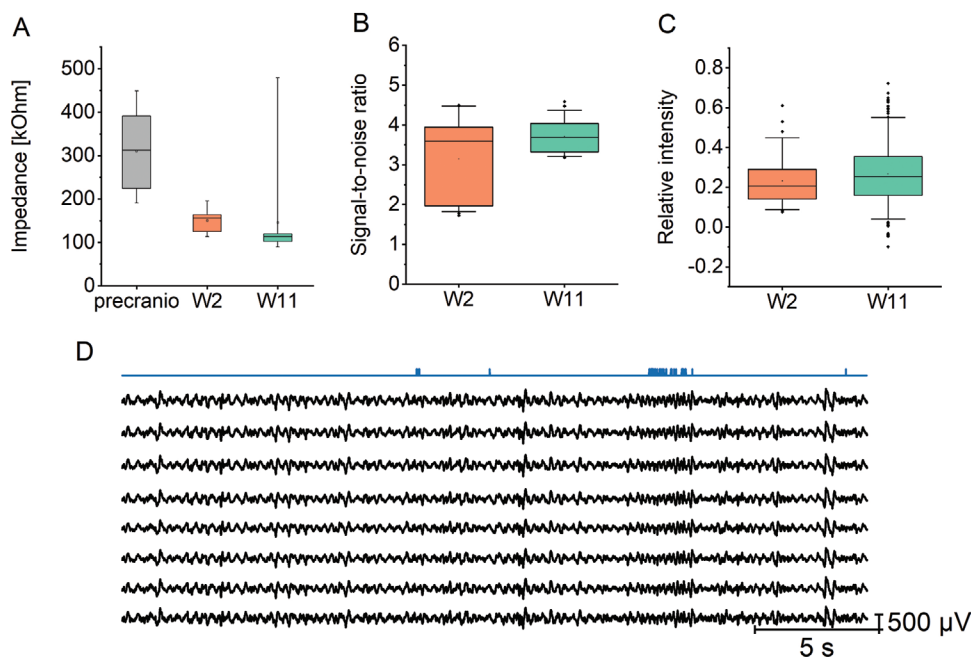


Figure 3. Measurements with Device A. A) Average impedance values of the channels ($n = 10$) on different measurement days at 1 kHz. B) Signal-to-noise ratio on the first ($n = 55$) and last ($n = 66$) measurement day. C) Long-term two-photon relative intensity change compared to the background intensity ($n_{W2} = 66$; $n_{W11} = 254$). The different boxes represent the different measurement days. Boxplot whiskers are 5th and 95th percentiles, and \blacklozenge are the outliers. D) 30 s long representative electrophysiological activity captured on W11 by the ECoG. The blue curve represents the movement of the animal.

experiment than for mice implanted with Device B. This was unrelated to the difference in the material composition of the devices.

In the case of Device B, the impedance of the functional electrodes increased not only after the surgery but also between week 1 and week 22 significantly (Student's paired sample t -test at $\alpha = 0.05$: $t(9) = -5.81$, $p \ll 0.05$), however, impedance still remained under 100 k Ω (Figure 4A). The moderate increase in the SNR was also visible in the case of the SIROF electrodes (Figure 4B).

We imaged awake, freely moving mice implanted with the μ ECoG device with a two-photon microscope using the CGaMP6f calcium indicator (Figure 5). Mice underwent two to three imaging sessions at different time points after implantation, over a period of 22 weeks at most. Labeled neurons were prominent on the initial measurements 1–2 weeks after implantation and this clear distinction from the background continued for the rest of the experiment (Figure 5).

We quantified this by calculating the intensity of automatically detected neurons compared to background fluorescence for each measurement day. Relative intensity change was not significantly different between measurement days in case of Device A (Student's t -test: $t(65) = -0.79$, $p = 0.43$). (Figure 3C). Although in the case of Device B there was a significant difference between the relative intensity values on different measurement days (one-way repeated measures analysis of variance [ANOVA] by OriginPro: $F(1.72, 96.15) = 16.99$, $p \ll 0.05$), the mean of the relative intensity stayed over 0.5 during the whole measurement period. (Figure 4C). Since imaging was performed with the same substrate material (thiol-ene/acrylate) in the light path in the case of both devices, we hypothesize

that the optical performance was influenced by other aspects, most likely suboptimal expression of GCaMP6f, and not by the μ ECoG device. Chronic imaging quality may be influenced by the immune response, sensor expression, and tissue regrowth, as well as factors introduced by the device. Nevertheless, cells also displayed spontaneous calcium activity often exceeding 50% increase in $\Delta F/F$, and the same cells were identifiable between measurements through 21 weeks (Figure 5).

To demonstrate the function of the ECoG device, representative electrophysiological activities were imaged (Figures 3D and 4D). The blue curves portray the movement of the mouse. Compare it with the activity curves motion originated activities can be observed.

4. Discussion

This study focuses on multimodal recordings with two-photon microscopy and presents the optical performance of a transparent SMP-based μ ECoG in chronically implanted mice.

The use of thiol-ene/acrylate as a SMP substrate material to create neural interfaces has only been exploited in the last few years.^[34] Probes implantable in the rodent brain have been proposed to perform intracortical recordings successfully.^[23,35,36] Long-term electrical stability of an SMP probe softening similarly to our substrate (from 2 Gpa to 300 Mpa) was investigated by Stiller et al., who found that impedance magnitude significantly decreased after 7 weeks but was found to not hinder recording capabilities up to 13 weeks. During that time period, SNR of their device was also maintained.^[35] In our study, both gold and SIROF electrodes on the same substrate exhibited

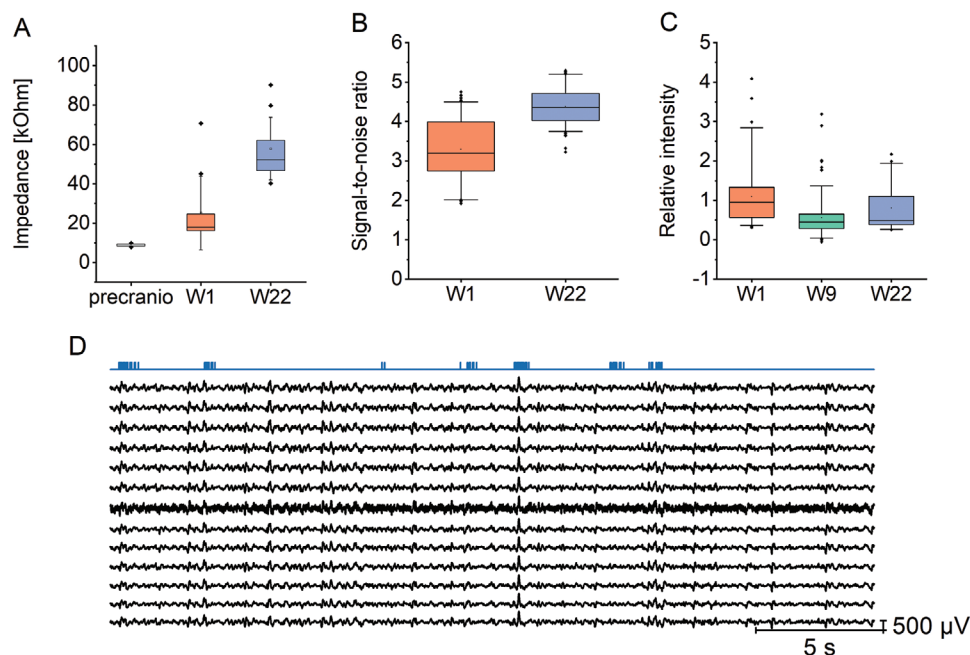


Figure 4. Measurements with Device B. A) Average impedance values of the channels ($n = 10$) on different measurement days at 1 kHz. B) Signal-to-noise ratio on the first ($n = 135$) and last measurement day ($n = 143$). C) Long-term two-photon intensity change of cells relative to background intensity ($n_{W1} = 67$; $n_{W22} = 57$). Box plots represent different measurement days. Boxplot whiskers are 5th and 95th percentiles, and \blacklozenge are the outliers. D) 30 long representative electrophysiological activity captured on W22 by the ECoG. The blue curve represents the movement of the animal.

significant change in impedance similarly, while showing a stable SNR during the 22-week long experiment. A similar trend was reported by another paper investigating the interface properties of an SMP neural probe softening from 2 GPa to 18 MPa in a 16-week long intracortical recording.^[35]

Both in vitro and in vivo studies have confirmed using histological methods that implantables made of SMP substrate evoke a less severe immune response compare to traditional silicon-based devices.^[19,23,30] Our group presented the application of this substrate to create an intracranial EEG electrode array for the first time.^[29] Based on the results of this fundamental work, we proposed here the operation of this implantable device to concurrently interrogate neuronal populations with electrical and optical approaches. Two-photon microscopy has evolved to be a primary in vivo tool for high spatial resolution fluorescence imaging in intact neural tissue. Compared with other imaging techniques, deeper imaging depths can be achieved due to the near-infrared excitation light, which is less scattered in the nervous tissue. Hence two-photon microscopy grants focal excitation localized to the focal volume, and there is no detectable off-focal fluorescence intensity to reject; images are obtained with higher contrast. Besides the advanced tissue-friendly feature of this SMP substrate already proved in prior studies, our data provides further evidence that two-photon imaging of fluorescently labeled cells through this transparent substrate is feasible at high spatial resolution. On hippocampal slices, we detected fine dendritic structures with the presented array in the light path without significant distortion in the two-photon microscope images.

Previous studies, where transparent multielectrode arrays were combined with fluorescent two-photon imaging, focused

on the proof-of-concept experiments, and did not address the longevity of optical properties or feasibility of simultaneous use of the optical and electrical recording in a longer period of time. Furthermore, image quality has not been monitored throughout experiments. To test the long-term optical performance of our device, we examined whether detected fluorescent calcium signals are of sufficient quality to distinguish between individual neuronal structures, with adequately performed long-term in vivo measurement at least up to 22 weeks after implantation. This period is relatively long, the latest transparent μ ECoG devices were only tested for a much shorter period. For instance, Thunemann et al. presented successful multimodal imaging through the positron emission tomography (PET)-based μ ECoG array in anaesthetized rats.^[18] In the work of Donahue et al., a Parylene C/PEDOT:PSS-based device was used to simultaneously monitor pathological activity in 4-Aminopyridine (4AP) induced acute epilepsy model.^[37] Driscoll et al. investigated induced epileptic seizures in acute experiments using a Parylene C/graphene MEA.^[19] Schweigmann et al. used a liquid crystal polymer (LCP)-based array for 28 days to capture GCaMP3 signals of neurons and astrocytes.^[38] Even though each of these studies reported on a novel material science approach to create a transparent MEA, none of these studies addressed the longevity of optical signals captured through these devices. Our group was first investigating the optical performance of such a transparent microdevice quantitatively, where a Parylene HT/ITO-based ECoG array was implanted and tested for 51 days.^[14] Based on our measurement result after 22 weeks, we found no sign of optical distortion that could be attributed to device failure. The optical performance of our transparent SMP μ ECoG arrays

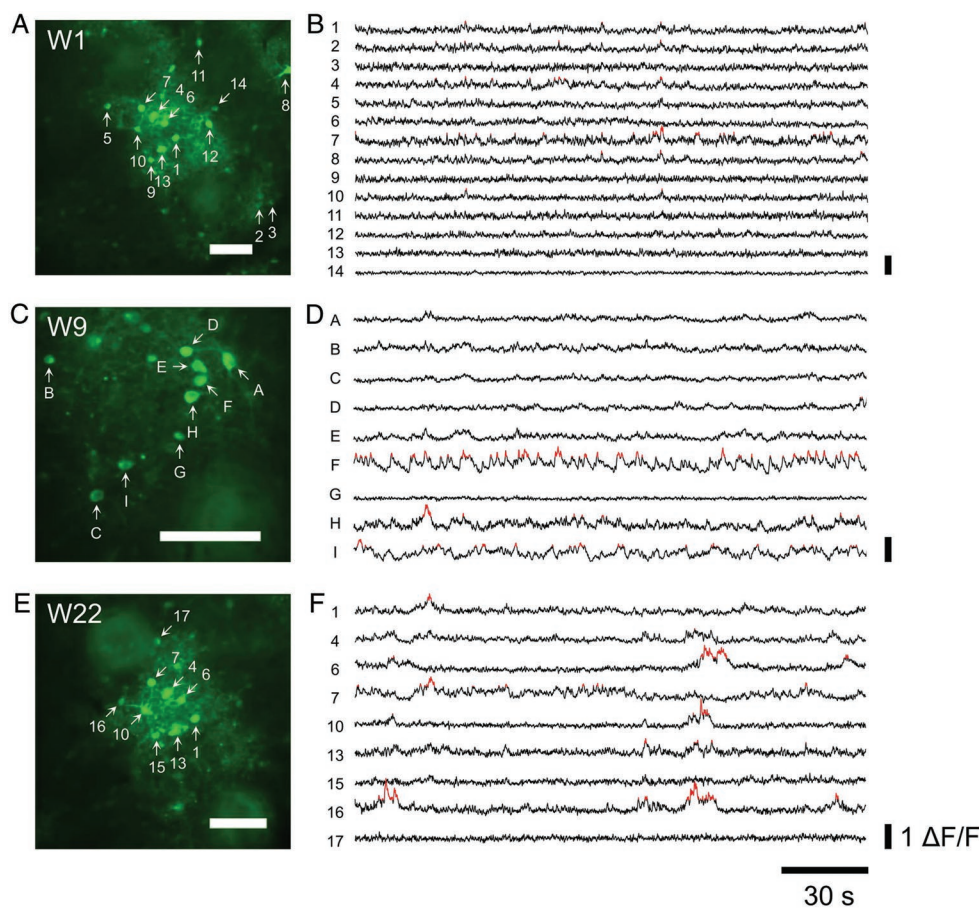


Figure 5. A,C,E) In vivo two-photon imaging field-of-view (scale bar: 100 μm) and B,D,F) spontaneous neural activity on different measurement days (Device B). A,B) 1 week post implantation. C,D) 9 weeks post implantation. E,F) 22 weeks post implantation. Images were recorded 150 μm below the brain surface. Field-of-view on (A) and (E) is identical, and numbers on (B) and (F) label activity of the same cells measured 1 and 22 weeks post implantation. On (B, D, F), $\Delta F/F$ increases of over 50% are highlighted in red.

undoubtedly meets the requirement of chronic experiments aiming for the synergetic use of two-photon microscopy and cortical electrophysiology.

Supporting Information

Supporting Information is available from the Wiley Online Library or from the author.

Acknowledgements

The authors are thankful to the National Brain Research Program (grant: 2017_1.2.1-NKP-2017-00002) and the Thematic Excellence Program (TKP2020-NKA-11, TKP2021-EGA-42). This work was supported by the grants KFI-2018-00097, VKE-2018-00032, and 712821-NEURAM for B.R. and by the National Research, Development and Innovation Fund (NKFIH FK 134403).

Conflict of Interest

The authors declare no conflict of interest.

Data Availability Statement

The data that support the findings of this study are available from the corresponding author upon reasonable request.

Keywords

implant materials, microECoG, neuroimaging, shape memory polymers, thiol-ene/acrylate

Received: April 1, 2022
Revised: June 2, 2022
Published online: August 2, 2022

- [1] M. Carter, J. C. Shieh, *Guide to Research Techniques in Neuroscience*, Academic Press, 2015.
- [2] Z. Fekete, A. Pongrácz, *Sens. Actuators, B* **2017**, 243, 1214.
- [3] F. Z. Fedor, A. Zátanyi, D. Cserpán, Z. Somogyvári, Z. Borhegyi, G. Juhász, Z. Fekete, *MethodsX* **2020**, 7, 101117.
- [4] G. Li, S. Wang, Y. Y. Duan, *Sens. Actuators, B* **2018**, 277, 250.
- [5] R. W. Tsien, R. Y. Tsien, *Annu. Rev. Cell Biol.* **1990**, 6, 715.
- [6] C. Stosiek, O. Garaschuk, K. Holthoff, A. Konnerth, *Proc. Natl. Acad. Sci. USA* **2003**, 100, 7319.

- [7] R. W. Tsien, R. Y. Tsien, *Annu. Rev. Cell Biol.* **2003**, *6*, 715.
- [8] K. Deisseroth, *Nat. Methods* **2010**, *8*, 26.
- [9] S. C. P. Williams, K. Deisseroth, *Proc. Natl. Acad. Sci. USA* **2013**, *110*, 16287.
- [10] S. M. Wellman, J. R. Eles, K. A. Ludwig, J. P. Seymour, N. J. Michelson, W. E. McFadden, A. L. Vazquez, T. D. Y. Kozai, *Adv. Funct. Mater.* **2018**, *28*, 1701269.
- [11] A. Zátanyi, Z. Borhegyi, M. Srivastava, D. Cserpán, Z. Somogyvári, Z. Kisvárday, Z. Fekete, *Sens. Actuators, B* **2018**, *273*, 519.
- [12] S. N. Obaid, R. T. Yin, J. Tian, Z. Chen, S. W. Chen, K. Benjamin Lee, N. Boyajian, A. N. Miniovich, I. R. Efimov, L. Lu, S. N. Obaid, R. T. Yin, J. Tian, Z. Chen, S. W. Chen, K. B. Lee, N. Boyajian, A. N. Miniovich, I. R. Efimov, L. Lu, *Adv. Funct. Mater.* **2020**, *30*, 1910027.
- [13] W. Yang, Y. Gong, C. Y. Yao, M. Shrestha, Y. Jia, Z. Qiu, Q. H. Fan, A. Weber, W. Li, *Lab Chip* **2021**, *21*, 1096.
- [14] A. Zátanyi, M. Madarász, O. Szabó, T. Lőrincz, R. Hodován, B. Rózsa, Z. Fekete, *J. Neural Eng.* **2020**, *17*, 016062.
- [15] A. F. Renz, J. Lee, K. Tybrandt, M. Brzezinski, D. A. Lorenzo, C. Cheraka, J. Lee, F. Helmchen, J. Vörös, C. M. Lewis, A. F. Renz, J. Lee, K. Tybrandt, M. Brzezinski, M. Cerra Cheraka, J. Vörös, D. A. Lorenzo, F. Helmchen, C. M. Lewis, *Adv. Healthcare Mater.* **2020**, *9*, 2000814.
- [16] S. Jeong, N. Choi, J. Ghim, J. H. Lee, H. J. Lee, J.-W. Seo, K. Kim, K.-W. Seo, M. Kyung Kim, S. Jeong, H. Kim, J.-W. Ghim, J. Ho Lee, N. Choi, J.-Y. Lee, H. J. Lee, J. Seo, K. Kim, K. Seo, J. Lee, *Adv. Funct. Mater.* **2020**, *30*, 2000896.
- [17] B. Lu, S. Zheng, B. Q. Quach, Y.-C. Tai, *Lab Chip* **2010**, *10*, 1826.
- [18] M. Thunemann, Y. Lu, X. Liu, K. Klill, M. Desjardins, M. Vandenberghe, S. Sadegh, P. A. Saisan, Q. Cheng, K. L. Weldy, H. Lyu, S. Djurovic, O. A. Andreassen, A. M. Dale, A. Devor, D. Kuzum, *Nat. Commun.* **2018**, *9*, 2035.
- [19] N. Driscoll, R. E. Rosch, B. B. Murphy, A. Ashourvan, R. Vishnubhotla, O. O. Dickens, A. T. C. Johnson, K. A. Davis, B. Litt, D. S. Bassett, H. Takano, F. Vitale, *Commun. Biol.* **2021**, *4*, 136.
- [20] D. Kuzum, H. Takano, E. Shim, J. C. Reed, H. Juul, A. G. Richardson, J. De Vries, H. Bink, M. A. Dichter, T. H. Lucas, D. A. Coulter, E. Cubukcu, B. Litt, *Nat. Commun.* **2014**, *5*, 5259.
- [21] Y. Lu, X. Liu, R. Hattori, C. Ren, X. Zhang, T. Komiyama, D. Kuzum, Y. Lu, X. Liu, D. Kuzum, R. Hattori, C. Ren, T. Komiyama, X. Zhang, *Adv. Funct. Mater.* **2018**, *28*, 1800002.
- [22] Y. Qiang, P. Artoni, K. J. Seo, S. Culaclii, V. Hogan, X. Zhao, Y. Zhong, X. Han, P. M. Wang, Y. K. Lo, Y. Li, H. A. Patel, Y. Huang, A. Sambangi, J. S. V. Chu, W. Liu, M. Fagiolini, H. Fang, *Sci. Adv.* **2018**, *4*, 0626.
- [23] A. Zátanyi, G. Orbán, R. Modi, G. Márton, D. Meszéna, I. Ulbert, A. Pongrácz, M. Ecker, W. E. Voit, A. Joshi-Imre, Z. Fekete, *Sci. Rep.* **2019**, *9*, 2321.
- [24] A. J. Shoffstall, M. Ecker, V. Danda, A. Joshi-Imre, A. Stiller, M. Yu, J. E. Paiz, E. Mancuso, H. W. Bedell, W. E. Voit, J. J. Pancrazio, J. R. Capadona, *Micromachines* **2018**, *9*, 486.
- [25] C. L. Frewin, M. Ecker, A. Joshi-Imre, J. Kamgue, J. Waddell, V. R. Danda, A. M. Stiller, W. E. Voit, J. J. Pancrazio, *Polymers* **2019**, *11*, 902.
- [26] N. A. Feidenhans'l, J. P. Lafleur, T. G. Jensen, J. P. Kutter, *Electrophoresis* **2014**, *35*, 282.
- [27] X. Xiao, X. Qiu, D. Kong, W. Zhang, Y. Liu, J. Leng, *Soft Matter* **2016**, *12*, 2894.
- [28] M. P. Gaj, A. Wei, C. Fuentes-Hernandez, Y. Zhang, R. Reit, W. Voit, S. R. Marder, B. Kippelen, *Org. Electron.* **2015**, *25*, 151.
- [29] F. Z. Fedor, M. Madarász, A. Zátanyi, Á. Szabó, T. Lőrincz, V. Danda, L. Spurgin, C. Manz, B. Rózsa, Z. Fekete, *Adv. Mater. Technol.* **2021**, *7*, 2100942.
- [30] B. Chiovini, D. Pálfi, M. Majoros, G. Juhász, G. Szalay, G. Katona, M. Szöri, O. Frigyesi, C. L. Haveland, G. Szabó, F. Erdélyi, Z. Máté, Z. Szadai, M. Madarász, M. Dékány, I. G. Csizmadia, E. Kovács, B. Rózsa, Z. Mucsi, *ACS Omega* **2021**, *6*, 15029.
- [31] T. J. Atherton, D. J. Kerbyson, *Image Vision Comput.* **1999**, *17*, 795.
- [32] D. Y. Huang, C. H. Wang, *Pattern Recognit. Lett.* **2009**, *30*, 275.
- [33] A. Lecomte, A. Degache, E. Descamps, L. Dahan, C. Bergaud, *Sens. Actuators, B* **2017**, *251*, 1001.
- [34] T. Ware, D. Simon, C. Liu, T. Musa, S. Vasudevan, A. Sloan, E. W. Keefer, R. L. Rennaker, W. Voit, *J. Biomed. Mater. Res., Part B* **2014**, *102*, 1.
- [35] A. M. Stiller, J. Usoro, C. L. Frewin, V. R. Danda, M. Ecker, A. Joshi-Imre, K. C. Musselman, W. Voit, R. Modi, J. J. Pancrazio, B. J. Black, *Micromachines* **2018**, *9*, 500.
- [36] A. M. Stiller, J. O. Usoro, J. Lawson, B. Araya, M. A. González-González, V. R. Danda, W. E. Voit, B. J. Black, J. J. Pancrazio, *Micromachines* **2020**, *11*, 619.
- [37] M. J. Donahue, A. Kaszas, G. F. Turi, B. Rózsa, A. Slézia, I. Vanzetta, G. Katona, C. Bernard, G. G. Malliaras, A. Williamson, *ENeuro* **2018**, *5*, 0187.
- [38] M. Schweigmann, L. C. Caudal, G. Stopper, A. Scheller, K. P. Koch, F. Kirchhoff, *Front. Cell. Neurosci.* **2021**, *15*, 308.